Composition Dependence of Microstructure, Phonon Modes, and Optical Properties in Rutile TiO_2:Fe Nanocrystalline Films Prepared by a Nonhydrolytic Sol−Gel Route

J. Z. Zhang, Y. D. Shen, Y. W. Li, Z. G. Hu,* and J. H. Chu

Key Laboratory of Polar Materials and Devices, Ministry of Education, Department of Electronic Engineering, East China Normal University, Shanghai 200241, People's Republic of China

Received: June 18, 2010; Revised Manuscript Received: August 7, 2010

Iron-doped titanium dioxide nanocrystalline (*nc*-TiO_2:Fe) films with the a composition from 2 to 10% have been deposited on Si(100) substrates by a facile nonhydrolytic sol−gel route. X-ray diffraction analysis shows that the films are polycrystalline and exhibit the pure tetragonal rutile phase structure. The Fe dopant effects on the surface morphology, microstructure, phonon modes, and dielectric functions of the *nc*-TiO_2:Fe films have been investigated by atomic force microscopy, ultraviolet Raman scattering, far-infrared reflectance, and spectroscopic ellipsometry at room temperature. With increasing Fe composition, the first-order Raman-active phonon modes E_g, A_{1g}, and B_{2g} are shifted toward a lower frequency side of 10, 6, and 7 cm^{-1}, respectively. The four additional vibrations, which are strongly related to the surface structure of the films, can be observed due to the two-phonon scattering process. Moreover, the three infrared-active transverse-optic (TO) phonon modes E_u (TO) can be located at about 183, 382, and 500 cm^{-1}, respectively. The dielectric functions of the films have been uniquely extracted by fitting the measured ellipsometric spectra with a four-phase layered model (air/surface rough layer/film/Si) in the photon energy range 0.73−4 eV (310−1700 nm). Adachi's dielectric function model has been successfully applied and reasonably describes the optical response behavior of the *nc*-TiO_2:Fe films from the near-infrared to ultraviolet photon energy region. It is found that the real part of dielectric functions in the transparent region slightly decreases with increasing Fe composition. Furthermore, the optical band gap linearly decreases from 3.43 to 3.39 eV with increasing Fe composition due to the energy level of Fe t_{2g}, which is closer to the valence band. It is believed that the decrease of the optical constants and optical band gap for the *nc*-TiO_2:Fe films with the Fe composition is mainly ascribed to the differences of the crystallinity and the electronic band structure, which can be perturbed by the transition metal introduction.

I. Introduction

Titanium dioxide (TiO_2) is a well-known material investigated due to its exceptional physical and chemical properties such as high dielectric constants, excellent optical transmittance in the near-infrared and visible region, high refractive index, ferromagnetism, ferroelectricity, low toxicity, pretty high energy density together with an excellent cycling life and photocatalysis for water cleavage.[1–6] Thus, it has been used in some applications, i.e., nonlinear optics, optoelectronic devices, negative electrodes, nanomedicine, chemical sensing, and catalysis.[7,8] As we know, TiO_2 is of three distinct polymorphs: rutile, anatase, and brookite. Both rutile and anatase are tetragonal, whereas brookite is orthorhombic. The Fermi level in the rutile phase is lower than that in the anatase phase by about 0.1 eV. The essential difference or advantage is that the rutile structure appears to have a narrower optical-absorption gap and higher thermodynamical stability than the others. There are many reports about the crystalline structure and electronic properties of TiO_2 bulk or film from both theoretical and experimental aspects.[9–13] Recently, Raman scattering and transmittance spectra have been used to investigate the first-order phonon modes and the optical response behavior of rutile TiO_2.[13,14] It was reported that the optical band gap (OBG) of rutile TiO_2 films on quartz substrates is about 3.6 eV,[14] which agrees well with the theoretical value of 3.6 ± 0.2 eV derived by the quasiparticle self-consistent GW approximation (G is Green's function, W is the screened Coulomb interaction).[15–17] Mo et al. reported the calculated band gap of rutile TiO_2 is 1.78 eV using the self-consistent orthogonalized linear combination of atomic orbitals method in the local density approximation (LDA).[18] It should be emphasized that the band gap is usually underestimated by the LDA method.[16,17] Therefore, more investigations are necessary to clarify the origin of deviation between theoretical and experimental results.

On the other hand, the discovery of ferromagnetism (FM) with Curie temperature above room temperature (RT) has been provided in Co-doped anatase TiO_2.[19] Many theoretical and experimental studies of 3d transition metal (V, Cr, Mn, Fe, Co, Ni, and Cu)-doped TiO_2 have been performed to testify the FM properties at RT.[20] Moreover, the antiferromagnetic coupling in the transition-metal-doped TiO_2 nanoparticle or nanocrystals has been recently reported. This can be explained by the fact that the 3d shells of them are half full or more.[21,22] Among all the dopants, the Fe element is frequently employed owing to its unique half filled electronic structure.[23] As we know, the introduction of transition metal can result in the variation of the electronic band structure for TiO_2 due to the sub-band formations in the forbidden gap. Therefore, studying the electronic transitions can provide valuable evidence for the FM and antiferromagnetic phenomena, which are strongly related to the transition metal doping. In addition, there are many

* Author to whom correspondence should be addressed. Phone: +86-21-54345150. Fax: +86-21-54345119. E-mail: zghu@ee.ecnu.edu.cn.

10.1021/jp1056286
Published on Web 08/19/2010

fabrication techniques adopted to prepare TiO_2-based films such as the sol−gel method, ion implantation, pulsed laser deposition, molecular beam epitaxy, chemical vapor deposition, and so on. Among them, the sol−gel technique is a well accepted method due to some superiorities: a fast fabrication process, large-area deposition, composition control, and low cost.[24] However, it is difficult to obtain nanostructured TiO_2 films with a uniformly dispersed Fe replacement due to the fast rate of hydrolysis via the traditional sol−gel method.[25,26] In the present work, a modified sol−gel technique was used to fabricate the homogeneous Fe-doped TiO_2 nanocrystalline (*nc*-TiO_2:Fe) films with the composition from 2 to 10%. This makes it possible to completely investigate the Fe-doping effects on the optical and electronic properties, which can provide insight on the energy levels from the Fe introduction.

There are many spectral techniques to determine the optical constants of film materials such as reflectance, transmittance, and spectroscopic ellipsometry (SE). Among them, SE based on the reflectance configuration is easily acceptable for the determination of optical constants.[24,27] It is a nondestructive and powerful technique that allows us to obtain the thickness and optical constants of a multilayer system without the Kramer−Kröning transformation (KKT) due to determining two independent angles simultaneously.[28] Note that SE can directly provide dielectric constants, optical band gap, optical conductivity, etc. Thus, this makes it possible to study the optical properties of TiO_2:Fe films in a wider photon energy range. In order to elucidate the distinguishing physical phenomena and further exploit the Fe-doped TiO_2 material as a viable candidate for fabricating optoelectronic and spinelectronic devices, the Fe-related optical properties should be thoroughly clarified and provide a critical reference to the device designs and performance optimizations.

In this paper, the surface morphology, microstructure, lattice vibrations, and optical properties of rutile TiO_2:Fe films deposited on Si(100) substrates with different Fe compositions have been investigated. The dielectric functions from the near-infrared to ultraviolet (NIR-UV) photon energy region have been studied by the SE technique. A theoretical model is presented to reproduce the experimental ellipsometric spectra. Effects of the Fe composition on the optical properties of *nc*-TiO_2:Fe films have been discussed in detail.

II. Experimental Details

Fabrication of *nc*-TiO_2:Fe Films. The *nc*-TiO_2:Fe films were deposited on Si(100) substrates by a facile nonhydrolytic sol−gel route employing a spin-coating process. In order to obtain the effects of Fe composition on the optical properties, the films were fabricated in the Fe composition range 2−10 mol % with the interval 2 mol %; i.e., the mole compositions of Fe atoms were 2, 4, 6, 8, and 10%, respectively. Analytically pure ferric nitrate ninehydrate ($Fe(NO_3)_3 \cdot 9H_2O$) and titanium butoxide ($Ti[O(CH_2)_3CH_3]_4$) were used as the starting materials. Titanium butoxide and an equimolar amount of acetylacetone were dissolved in ethanol. The Fe doping was achieved by dissolving ferric nitrate ninehydrate in the solution with a required volume ratio of CH_3CH_2OH:CH_3COOH. Then, the two solutions were mixed together at a certain temperature and allowed to stir for 2 h at 50 °C to increase the homogeneity. The amount of Fe doping was denoted as the fraction (%) number of Fe atoms to the sum of those of Ti and Fe atoms in the precursor solution. Finally, the 0.3 M precursor solution was transparent without precipitate phenomenon after several months. Note that the distilled water, which quickly reacts with titanium butoxide, is not used in the present method, as compared to the traditional hydrolysis technique.[25] The Si(100) substrates were cleaned in pure ethanol with an ultrasonic bath to remove physisorbed organic molecules from the surfaces. Then, the substrates were rinsed several times with deionized water. Finally, the wafers were dried in a pure nitrogen stream before the deposition of the films. The TiO_2:Fe films were deposited by spin coating of the 0.3 M solution onto the substrates at a speed of 4000 rpm for 30 s. Each layer of the films was dried at 200 °C for 3 min, then pyrolyzed at 400 °C for 4 min to remove residual organic compounds, and then annealed at 850 °C for 4 min in ambient air by a rapid thermal annealing procedure. The deposition and annealing-treatment procedures were repeated five times to obtain the desired thickness.

XRD, AFM, UV Raman, FIR Reflectance, and SE Measurements. The crystalline structure of the TiO_2:Fe films was investigated by X-ray diffraction (XRD) using a Ni filtered Cu Kα radiation source (D/MAX- 2550 V, Rigaku Co.). In the XRD measurement, a vertical goniometer (model RINT2000) was used and the continuous scanning mode ($\theta - 2\theta$) was selected with a scanning rate of 10°/min and an interval of 0.02°.[24] The surface morphology was investigated by atomic force microscopy (AFM) with the contacting mode in areas of $5 \times 5\ \mu m^2$ (Digital Instruments Dimension 3100, Veeco). Ultraviolet (UV) Raman scattering experiments were carried out by a micro-Raman spectrometer with a spectral resolution of 1.5 cm^{-1} (Jobin-Yvon LabRAM HR 800 UV). The 325 nm (3.82 eV) line of a He−Cd laser was applied as an excited source with an output of 30 mW.[29] Far-infrared (FIR) reflectance spectra of the films were collected using a Bruker Vertex 80 V Fourier transform infrared (FTIR) spectrometer over the wavenumber range 100−700 cm^{-1}. A TGS/POLY detector and 6-μm-thick mylar beamsplitter were employed for the spectral measurement. Near-normal incident reflectance (about 10°) was recorded with a spectral resolution of 2 cm^{-1}. An aluminum mirror, whose absolute reflectance was measured, was taken as the reference for the reflectance spectra in the FIR region.[30] The illuminated area on the film surface was estimated to be about 4 mm in diameter. The ellipsometric measurements were recorded by a NIR-UV SE in the wavelength range 310−1700 nm (0.73−4.0 eV) with a spectral resolution of 2 nm (SC630UVN by Shanghai Sanco Instrument, Co., Ltd.).[31] The incident angle was selected to 70° for the *nc*-TiO_2:Fe films corresponding to the experimental optimization near the Brewster angle of the Si substrate. Note that the films were at RT for all measurements and no mathematical smoothing has been performed for the experimental data.

III. Results and Discussion

Structural and Morphology Characterizations. The XRD patterns of the TiO_2:Fe films with different Fe compositions deposited on Si(100) are shown in Figure 1. It can be seen that all the films are polycrystalline with a stronger (110) diffraction peak, whose position is shifted from 27.5 to 27.7° with the Fe composition. The phenomena can be explained by the fact that the radius of Fe atom is larger than that of Ti atom. Besides the strong feature, there are several other weaker diffraction peaks, (111), (211), and (220), and no impurity phase is observed, which confirms that the films are of the pure rutile structure. It suggests that the polycrystalline grains with different orientations are formed in the rutile films and the Fe atoms have been successfully incorporated into the TiO_2 matrix. On the basis of the (110) diffraction peak, the lattice constant *a* of the Fe-doped films is estimated and varied between 4.553 and 4.590 Å. The

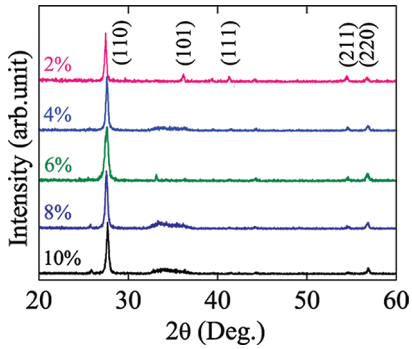

Figure 1. The XRD patterns of the TiO_2:Fe films grown on Si(100) substrates with the Fe compositions of 2, 4, 6, 8, and 10%, respectively.

TABLE 1: The Peak Position and Full Width at Half-Maximum (FWHM) of the (110) Diffraction Peak of *nc*-TiO_2:Fe Films with the Fe Compositions (C_{Fe}) Determined from the XRD Patterns in Figure 1

samples	C_{Fe} (%)	peak position, 2θ (deg)	fwhm, β (deg)	lattice constant, a (Å)	grain size, r (nm)
A	2	27.5	0.28	4.590	29
B	4	27.6	0.32	4.565	26
C	6	27.6	0.48	4.573	17
D	8	27.6	0.34	4.574	24
E	10	27.7	0.35	4.553	24

differences of the lattice constant suggest that there are different lattice distortions in the rutile films with increasing Fe composition. Furthermore, the average crystalline size r can be calculated from the (110) peak according to the well-known Scherrer equation: $r = (K\lambda)/(\beta \cos \theta)$. Here, $K \approx 1$ is the shape factor, $\lambda = 1.540$ Å the X-ray wavelength of Cu Kα radiation, β the line broadening at full width at half-maximum (fwhm) in degrees, and θ the Bragg diffraction angle.[32,24] From Table 1, the grain size (about 17 nm) of *nc*-TiO_2:Fe film with the composition of 6% is the smallest due to a much larger value of β. On the other hand, the film doped with the composition of 2% has the largest root-mean-square roughness, which can be estimated to about 5 nm and the others are of about 3 nm from Figure 2. Moreover, from the section of the three-dimension AFM pictures, the grain size of the films can be qualitatively defined,[33,34] which confirms that the grain size of the film doped with the composition of 2% is the largest among the films, which agrees with that of the XRD patterns. As can been seen in Figure 2, the surface morphology presents a different pattern with the Fe doping. The film surface becomes more dense with increasing Fe composition, which indicates that few voids appear on the surface. The large variation can obviously affect the lattice vibrations and optical properties of the films, such as second-order Raman-active frequencies, high frequency dielectric constants, and optical band gap discussed in the following.

Raman and Far-Infrared Spectra. Generally, rutile TiO_2 belongs to the tetragonal structure (space group D_{4h}^{14}, or $P4_2/mnm$) with two units and shows four first-order Raman-active modes ($B_{1g} + E_g + A_{1g} + B_{2g}$), four fundamental infrared-active modes ($A_{2u} + 3E_u$), and three main silent modes ($2B_{1u} + A_{2g}$) at the Γ point of the Brillouin zone (BZ).[4,35] The B_{1u} mode located at 113 cm^{-1} and other optical inactive modes usually occurring at lower frequencies cannot be observed due to the experimental limitation in the present work. The Raman-active and infrared-active phonon modes of rutile TiO_2:Fe films with different Fe compositions are shown in Figure 3a and b,

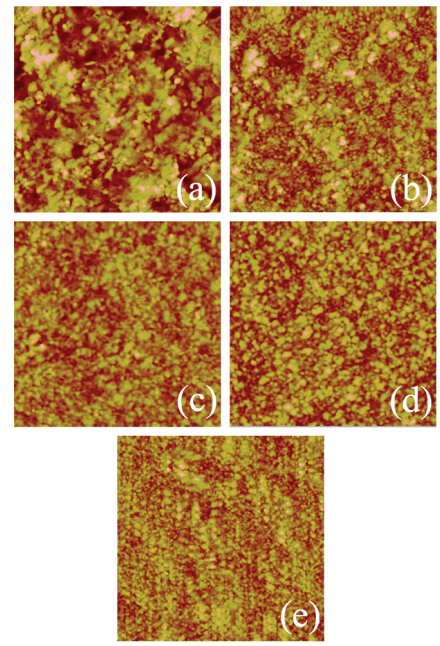

Figure 2. AFM two-dimensional images of the TiO_2:Fe films with the Fe compositions of (a) 2, (b) 4, (c) 6, (d) 8, and (e) 10%, respectively. Note that the scale height is 40 nm and the measured area is 5 × 5 μm^2.

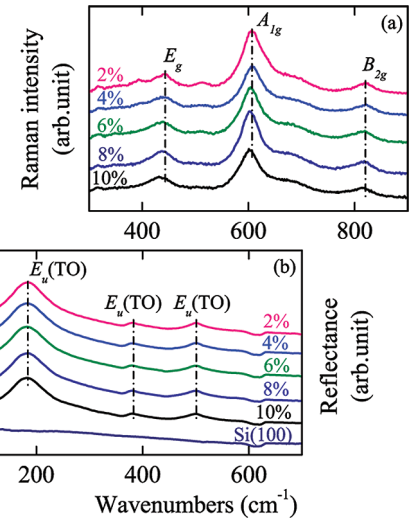

Figure 3. (a) Raman spectra of the TiO_2:Fe films under the excitation line of 325 nm. (b) The FIR reflectance spectra of the TiO_2:Fe films with different Fe compositions. The infrared reflectance of the Si(100) substrate is shown as a reference. The dashed lines show the positions of Raman-active and infrared-active phonon modes.

respectively. The fundamental Raman modes E_g, A_{1g}, and B_{2g} and main infrared modes $3E_u$ can be readily recognized. In addition, there are some second-order Raman scattering features in Figure 3a and the most prominent one is located at about 680 cm^{-1}, which appears with a shoulder structure. From the Raman and FIR reflectance spectra, it further confirms that the TiO_2:Fe films are of the pure rutile phase and no anatase or brookite impurities are detected. The three Raman modes for rutile TiO_2 are found at about 447, 612, and 827 cm^{-1}, which can be uniquely corresponding to E_g, A_{1g}, and B_{2g}, respectively. The intensity and peak positions of the above Raman-active phonon modes are in good agreement with the experimental data reported for the pure rutile compound.[14,36] It can be seen that the peak positions of Raman modes from the Fe-doped TiO_2 films are shifted toward a lower frequency side as compared to

the pure TiO_2 reported. The intensity of the A_{1g} band is stronger than those of the E_g and B_{2g} bands because the A_{1g} phonon mode is easily resonance enhanced when the laser line of 325 nm is selected owing to the UV resonance Raman effect.[36] Moreover, the A_{1g} phonon mode arising from oxygen vibrations has a negatively sloping branch along (110) and a flat branch along the (100) direction, both lying in the plane of Ti−O stretch.[12] Therefore, the A_{1g} vibration band can provide an obvious effect due to the crystalline orientation of *nc*-TiO_2:Fe films because the (110) diffraction peak is the strongest from the XRD patterns.

For four main infrared-active phonon modes, the experimental positions of transverse-optical (TO) and longitudinal-optical (LO) phonon frequencies from single crystal TiO_2 are located at 183 cm^{-1} (TO), 373 cm^{-1} (LO), 388 cm^{-1} (TO), 458 cm^{-1} (LO), 500 cm^{-1} (TO), and 807 cm^{-1} (LO) for $3E_u$ (Γ_5^+) and at 167 cm^{-1} (TO) and 812 cm^{-1} (LO) for A_{2u} (Γ_1^-), respectively. The oscillator strength vectors for the $3E_u$ modes belong to the $x-y$ plane, i.e., $\vec{q} = (q_x, q_y, 0)$. However, the phonon wave vector $\vec{q}$ for the A_{2u} mode is along the z or c axis ([001] direction). The intensity and peak positions of the infrared-active phonon modes $3E_u$ (TO) are shown in Figure 3b. The phonon frequencies can be located at about 183, 382, and 500 cm^{-1}, which are close to those found in single crystal TiO_2. It should be emphasized that the band at 382 cm^{-1} is softened by 6 cm^{-1} and the broadening of the mode 183 cm^{-1} is the largest among the $3E_u$ (TO) phonon modes. It can be ascribed to the lattice mismatch between film and substrate and lattice defects in the TiO_2:Fe films. The infrared spectral lineshapes corresponding to different Fe compositions are similar due to the low-composition doping, which cannot strikingly contribute to the phonon characteristics. Note that only the E_u (TO) phonon modes can be observed in the present experimental configuration, where the LO and A_{2u} vibrations are not responsive to the unpolarized light incidence. The phenomena can be explained as follows: (i) the E_u (TO) phonon modes are active for light polarized perpendicular to the c crystallographic axis, and (ii) the films show the single rutile phase and the normal line on the sample surface is parallel or subparallel to the c axis.[37] In addition, the A_{2u} phonon frequency can be decreased to zero by applying a uniaxial expansive strain due to the Fe doping in the (001) direction.[1] Moreover, the LO−TO splitting, which is due to the coupling between infrared-active modes and macroscopic electric fields, can result in a high frequency of the corresponding LO phonon mode and the broadening LO phonon−plasmon (LPP) coupled modes.[4,37] Generally, the E_u (LO) phonon modes can appear when the polarized light parallel to the incident plane and/or the larger incident angle are applied. Nevertheless, the optical anisotropic effect will become weaker owing to the polycrystalline structure of *nc*-TiO_2:Fe films. It can be concluded that the frequency shifts of the Raman modes are sensitive to the Fe doping and the broadening of the infrared-active modes is sensitive to the lattice mismatch and intracrystalline defects.

Lattice Vibrations. In order to further study the lattice vibrations and microstructure, Figure 4 presents a seven-peak fit of the Raman spectra recorded in the range 300−900 cm^{-1} for *nc*-TiO_2:Fe films with different Fe compositions. The Lorentzian multipeak fitting including three first-order Raman-active phonon modes (E_g, A_{1g}, and B_{2g}), the combination mode at about 680 cm^{-1}, and three additional modes at about 320, 390 or 360, and 510 cm^{-1} is required to describe the profile satisfactorily. The four additional features are from the two-phonon scattering process, which can be seen in the σ_{zz} polarizability component for bulk rutile.[12] It is noted that σ is

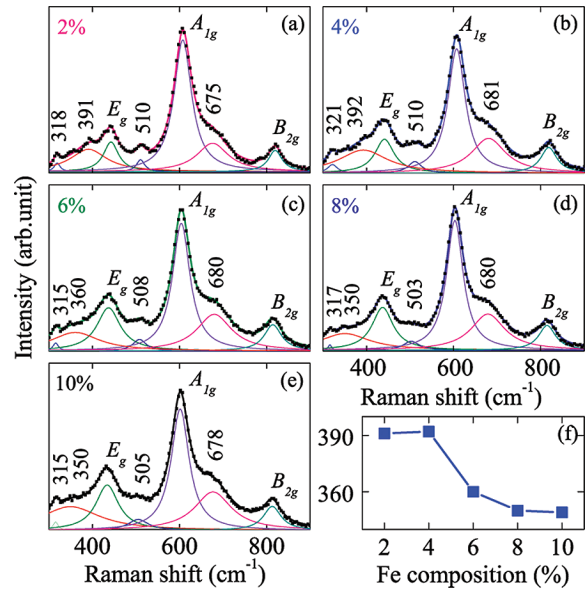

Figure 4. A seven-peak fit of the Raman spectra for the TiO_2:Fe films with the compositions of (a) 2, (b) 4, (c) 6, (d) 8, and (e) 10%, respectively. The three first-order and four second-order Raman phonon modes are indicated. (f) An additional vibration at about 350−390 cm^{-1} is varied as the Fe composition.

a scattering tensor and σ_{zz} is a nonzero tensor element. The stress-induced effects from the lattice mismatch with the Si substrates and phonon dispersion relation may be responsible for the observed second-order Raman-active phonon modes.[12,29] Moreover, when a rutile structure is truncated with a plane perpendicular to the (110) direction, the 4-fold axis is lost to yield C_{2v} symmetry. Nomoto et al. assigned the band at about 510 cm^{-1} to one degenerated E_u (TO) phonon mode with B_2 symmetry on the surface and the band at around 360 cm^{-1} to the A_1 derived from the E_u (LO) phonon mode. The fact that the displacements of O atoms are in the opposite direction to the displacements of the Ti atoms can induce the additional vibration mode at about 360 cm^{-1}, which can be the polar mode toward the surface normal.[38] As shown in Figure 3f, the additional vibration mode located at about 350−390 cm^{-1} is softened with increasing Fe composition. It means that the surface structure of the films is perturbed by the Fe introduction. In addition, the phenomena could be affected by the different grain size and surface morphology according to the XRD patterns and AFM images. Therefore, the appearing of the additional vibration modes could be attributed to the Fe composition, grain size, and surface morphology.

As seen in Figure 5, the composition dependence of Raman-active modes E_g, A_{1g}, and B_{2g} can be well expressed by $(450-177x)$, $(610-102x)$, and $(824-87x)$ cm^{-1}, respectively. It suggests that the Raman phonon frequencies are shifted toward a lower frequency side of about 10, 6, and 7 cm^{-1}, respectively. There are some factors, such as the phonon confinement model (PCM), internal stress/surface tension effects, and oxygen vacancies, that can result in the Raman spectral modifications observed in the TiO_2:Fe films. Parker et al. reported that the redshift of the E_g phonon mode was due to the nonstoichiometric effects.[39] In the present case, the thermal treatment was carried out at 850° in ambient air and the oxygen vacancies can be negligible. Thus, we can conclude that the observed shifts in the phonon frequencies are not affected by the nonstoichiometric effects, i.e., oxygen vacancies. As we know, the translational invariance is markedly broken when the crystal extension is in the dimension range 1−100 nm. In this case, a description of

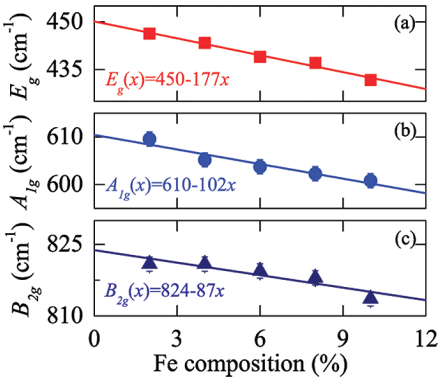

Figure 5. Fe composition dependence of the (a) E_g, (b) A_{1g}, and (c) B_{2g} phonon modes for the TiO_2:Fe films. Note that the solid lines are the linear fitting results to guide the eyes.

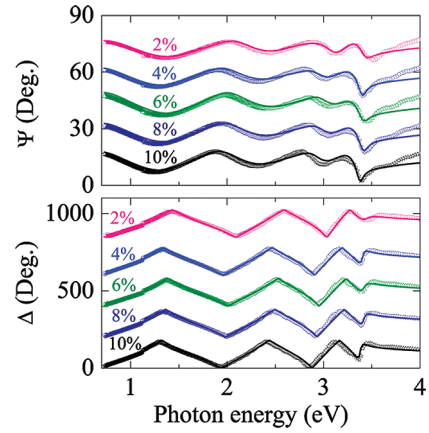

Figure 6. NIR-UV experimental (dotted lines) and best-fitted ellipsometric (solid lines) spectra of the TiO_2:Fe films with the Fe compositions of 2, 4, 6, 8, and 10%, respectively. For clarity, each spectrum of Ψ and Δ is shifted by 15 and 200°, respectively.

lattice vibrations in such a domain in terms of phonons with a well-defined wave vector is no longer valid.[40] Hence, the confinement of phonons by finite-sized rutile crystallites has been posited as the most convincing proposal.[35] According to the PCM principle, a negative phonon dispersion away from the BZ center may result in asymmetric low-frequency broadening and redshift.[12,13] Compared with the grain sizes extracted from the XRD patterns (Table 1), however, the PCM theory is not adequate enough to explain the features of the lattice vibrations due to the various grain sizes of *nc*-TiO_2:Fe films. The present results suggest that the redshifts of the first-order Raman-active phonon frequencies in the TiO_2:Fe films are modified by the Fe-doping perturbation. To fully explain the redshifts of the E_g, A_{1g}, and B_{2g} phonon modes, it must be taken into account that the ionic radius of the Fe^{3+} ion (0.645 Å) is significantly larger than that of the Ti^{4+} one (0.605 Å).[41] Hence, the microstructure of *nc*-TiO_2:Fe films is slightly changed by the substitutions of Fe ions, which induces the redshifts of three Raman-active phonon modes. In addition, it indicates that the Ti lattice position is partly occupied by the Fe dopant and the replacement is indeed realized in the TiO_2 matrix.

SE Theoretical Consideration. SE, based on the reflectance configuration, provides an effective tool to extract simultaneously thickness and optical constants of a multilayer system.[24,42] It is a sensitive and nondestructive optical method that measures the relative changes in the amplitude and the phase of particular directions of polarized light upon oblique reflection from the sample surface. The experimental quantities measured by ellipsometry are the complex ratio $\tilde{\rho}(E)$ in terms of the angles $\Psi(E)$ and $\Delta(E)$, which are related to the structure and optical characterization of materials and defined as $\tilde{\rho}(E) \equiv \tilde{r}_p(E)/\tilde{r}_s(E) = \tan \Psi(E)e^{i\Delta(E)}$; here, $\tilde{r}_p(E)$ and $\tilde{r}_s(E)$ are the complex reflection coefficients of the light polarized parallel and perpendicular to the incident plane, respectively.[28] It should be noted that $\tilde{\rho}(E)$ is the function of the incident angle, the photon energy E, film thickness and optical constants $\tilde{n}(E)$, i.e., the refractive index n and extinction coefficient κ from the system studied. Although $\tilde{\rho}(E)$ and $\tilde{n}(E)$ may be transformed, there are no corresponding expressions for $\tilde{n}(E)$, which is distinct for different materials.[43] Therefore, the spectral dependencies of $\Psi(E)$ and $\Delta(E)$ have to be analyzed using an appropriate fitting model. The film thickness d_f, optical constants, and other basic physical parameters, such as OBG E_{OBG}, the high frequency dielectric constant ε_∞, etc., can be extracted from the best fit between the experimental and fitted spectra.

In order to extract the dielectric functions and other physical parameters of the rutile TiO_2:Fe films on the Si substrates, the SE spectra were analyzed by a multilayer model with the four-phase layered structure (air/surface rough layer (SRL)/film/substrate). It should be noted that the reliability of the fitting method mainly depends on the selection of the dielectric function model. For direct wide band gap semiconductor materials, the dielectric functions $\tilde{\varepsilon}(E) = \varepsilon_1(E) + i\varepsilon_2(E)$ at energies below and above the fundamental band gap can be calculated by Adachi's model, which is based on the KKT and strongly connected with the electronic band structure of materials. The method reveals the distinct structures at the energy of the three-dimensional M_0-type critical point E_{OBG}, which is written as

$$\tilde{\varepsilon}(E) = \varepsilon_\infty + \frac{A_0[2 - \sqrt{1 + \chi_0(E)} - \sqrt{1 - \chi_0(E)}]}{\sqrt{E_{OBG}^3 \chi_0(E)^2}} \quad (1)$$

where $\chi_0 = (E + i\Gamma)/E_{OBG}$ and A_0 and Γ are the strength and broadening values of the E_{OBG} transition, respectively.[44] The above Adachi model is successfully employed in many semiconductor and dielectric materials.[14,29,30] Correspondingly, the optical constants $\tilde{n}(E) = n(E) + i\kappa(E)$ can be calculated from the well-known relationship $\tilde{n}(E) = [\tilde{\varepsilon}(E)]^{1/2}$. The Brüggeman effective medium approximation was employed to calculate the effective dielectric functions of SRL.[45,46] In the present case, the SRL is described by the assumption 50% void component and 50% TiO_2:Fe component. It should be emphasized that the fixed mixture ratio 50%−50% is reasonable because the deviation from the value of 0.5 is small and can be negligible. The dielectric functions of the void component are taken to be unity. The optical constants of the Si substrate in the fitting process can be directly taken from ref 47. The best-fit parameter values in eq 1 can be obtained by the Levenberg−Marquardt algorithm in the linear least-squares curve fitting.[48] The root-mean-square fractional error function has been used to judge the fitting quality between the experimental and modeled data.

Ellipsometric Spectra. The experimental $\Psi(E)$ and $\Delta(E)$ spectra recorded at an incident angle of 70° for the TiO_2:Fe films on Si(100) substrates are shown by the dotted lines in Figure 6. The interference patterns due to the finite thickness of films are observed below the photon energy of about 3.2 eV, indicating that the films are transparent in the photon energy region. The dielectric functions of the films can be determined by fitting Adachi's dielectric function model to the measured data. The fitted parameter values in eq 1 and thicknesses of

TABLE 2: The Parameter Values of Adachi's Dielectric Function Model for *nc*-TiO_2:Fe Films with the Fe Compositions (C_{Fe}) Determined from the Simulation of Ellipsometric Spectra in Figure 6

samples	C_{Fe} (%)	ε_∞	A_0 ($eV^{3/2}$)	E_{OBG} (eV)	Γ (eV)	d_s (nm)	d_f (nm)
A	2	0.07	151	3.43	0.09	2	181
B	4	0.37	141	3.42	0.08	1	198
C	6	0.46	130	3.40	0.09	1	198
D	8	0.42	137	3.42	0.08	1	197
E	10	0.63	130	3.39	0.07	2	202

both SRL d_s and films d_f are summarized in Table 2, and the simulated ellipsometric spectra for *nc*-TiO_2:Fe films are shown by the solid lines in Figure 6. As can be seen, a good agreement is obtained between the experimental and calculated spectra in the entirely measured photon energy range. However, some deviations at higher photon energy in the curve fit from the experimental $\Psi(E)$ data are observed because it is a strong absorption region, which is beyond the lowest direct gap E_{OBG}. The grain boundaries and surface morphologies of the polycrystalline films would affect the detected polarized light. Nevertheless, the factors such as the polycrystalline, anisotropy, and boundaries are not considered in the fit program owing to the intrinsic complexity. This can affect the measured ellipsometric parameter values and deteriorate the fit. It should be noted that a small band near 1100 nm (1.13 eV) is removed from the measured data due to an absorption band of the optical fiber. From Table 2, the thickness of the TiO_2:Fe films including the SRL and film layer is estimated to be 183, 199, 199, 198, and 204 nm with increasing Fe composition, respectively. Note that the results agree well with the nominal growth value of about 200 nm. Therefore, it is verified that the fitting model used is adequate to describe the dispersion relation of the NIR-UV optical properties of the *nc*-TiO_2:Fe films. On the other hand, it also indicates that the effects of different thicknesses on the optical properties of the films can be neglected.

NIR-UV Dielectric Functions and Optical Band Gap. The evaluated real and imaginary parts of dielectric functions $\tilde{\varepsilon}(E)$ of the TiO_2:Fe films are shown in Figure 7a and b, respectively. $\varepsilon_1(E)$ and $\varepsilon_2(E)$ with the photon energy are the typical optical response behaviors of semiconductor and/or dielectric materials.[10,28,47] Generally, with increasing photon energy, $\varepsilon_1(E)$ increases and approaches the maximum of 11 at about 3.5 eV and then decreases due to the well-known Van Hove singularities. It was reported that a higher $\varepsilon_1(E)$ is shown to be a consequence of a low-frequency, "soft" phonon mode and large Born effective charges, as confirmed by Raman and FIR reflectance spectra.[1] In the transparent region ($E < E_{OBG}$), $\varepsilon_2(E)$ is close to zero and remarkably increases as the photon energy further increases beyond E_{OBG}. It indicates that a strong optical absorption appears, showing the interband electronic transition from the valence band (VB) to the lowest conductive band (CB). Moreover, all the absorption edges from $\varepsilon_2(E)$ are not much sharper because there are the Urbach tail states.[14] The Urbach tail feature can be expressed by the following rule as $\alpha = \alpha_0 \exp(E/E_u)$; here, α is the absorption coefficient, α_0 is a constant, and E_u is the Urbach energy.[49] The parameter E_u can be strongly related to the width of the tails of localized states in the band gap. The absorption in the region is mainly due to transitions between extended states in one band and localized states in the exponential tail of the other band.[50] Therefore, the explanation for the appearance of the Urbach tail is the ionization of excitons by internal electric microfields, which is produced by the crystalline defects, charged impurities, grain boundaries, and lattice disorder in the TiO_2:Fe films.

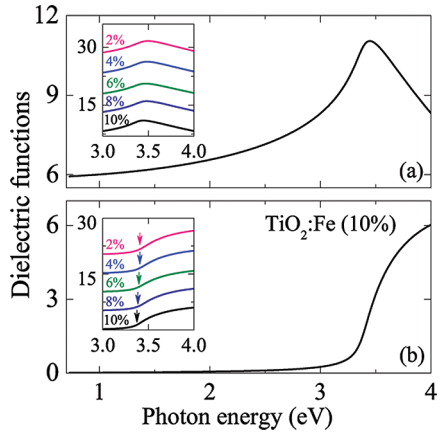

Figure 7. Evolution of the real part ε_1 (a) and imaginary part ε_2 (b) of dielectric functions for the TiO_2:Fe film with the Fe composition of 10% in the photon energy range from 0.73 to 4 eV. Note that the insets show the dielectric functions of the TiO_2:Fe films in an enlarged photon energy region of 3−4 eV. The arrows indicate the absorption edge shift.

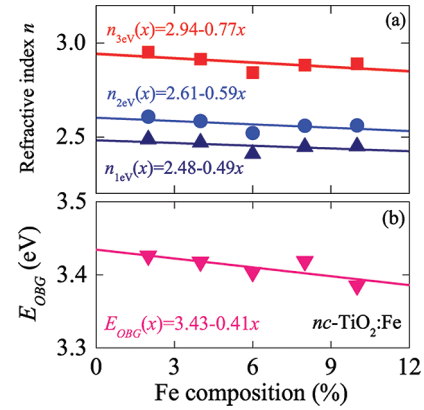

Figure 8. Composition dependence of (a) the refractive index n at three photon energies of 1, 2, and 3 eV and (b) the optical band gap E_{OBG} for the *nc*-TiO_2:Fe films, respectively. The solid lines represent the linear fitting results.

Figure 8a shows the variations of the refractive index $n(x)$ as a function of the Fe composition at photon energies of 1, 2, and 3 eV, respectively. The change trend can be well expressed by the linear relationship $(2.48-0.49x)$, $(2.61-0.59x)$, and $(2.94-0.77x)$, respectively. It suggests that the refractive index linearly decreases with the Fe composition in the visible region. It should be emphasized that the deviation of the TiO_2:Fe film with the composition of 6% may be due to the smallest grain size. The discrepancy of the grain size could result in the film density variations, which induces a lower refractive index.[14] The model parameters and fitted values for the E_{OBG} are shown in Figure 8b by the dotted and solid lines, respectively. It indicates that E_{OBG} decreases with the Fe composition from 2 to 10%. In pure rutile films, the electronic band structure is due to the electrostatic and crystal-field interaction between O_{2p} ionic orbitals.[14] In particular, there is a substantial degree of hybridization between O_{2p} and Ti_{3d} orbitals in both the CB and VB regions, indicating the excitation across the band gap involves both O_{2p} and Ti_{3d} states. It should be noted that the lowest CB consists of two sets of Ti_{3d} bands, which have their atomic origin from the hybridized states of t_{2g} and e_g. E_{OBG} of rutile TiO_2 is assigned to the interband transition from the highest VB to the lowest CB.[16] In rutile Fe-doped TiO_2, Fe dopant can affect the

E_{OBG} of *nc*-TiO_2 films by acting as hole (or electron) traps and by altering the h^+/e^- pair recombination through the following process:[51]

$$h\nu + Fe^{3+} + h^+_{VB} \rightarrow Fe^{4+} \qquad \text{hole trap} \qquad (2a)$$

$$Ti^{4+} + e^-_{CB} \rightarrow Ti^{3+} + h\nu \qquad \text{electron trap} \qquad (2b)$$

where the energy level for Fe t_{2g} is close to the VB edge and the energy level for Ti^{4+} is located in the CB. Introduction of such an energy level (Fe t_{2g}) in the band gap induces the redshift of E_{OBG} through a charge transfer between a dopant and the CB or a d−d transition in the crystal field. According to the energy level discussed previously, about 40 meV shift of the E_{OBG} in the Fe-doped TiO_2 films can be attributed to the charge-transfer transition from the d orbital of the Fe ion to the CB. The hole-compensated Fe^{4+} is presumed to act as a hole trap and the charge-compensated Ti^{3+}, as an electron trap.[52,23] Finally, Figure 8b shows the composition dependence of E_{OBG}, which may be expressed in the form $(3.434-0.404x)$ eV. It indicates that E_{OBG} slightly decreases with increasing Fe composition. It can be suggested that the E_{OBG} value of pure rutile TiO_2 films is about 3.434 eV from the linear fitting, which is slightly smaller than the reported value of 3.6 eV.[14] It should be noted that the values are less than that derived by the theoretical calculation.[16,17] The difference of E_{OBG} could be due to the dopant composition, the d electronic configuration, and the electron donor composition of the *nc*-TiO_2:Fe films.

IV. Conclusion

To summarize, the *nc*-TiO_2:Fe films have been deposited on Si(100) substrates by a facile nonhydrolytic sol−gel route. All of the films are polycrystalline with a stronger (110) diffraction peak, and the film surface becomes more dense with increasing Fe composition. The Fe composition dependence of the lattice vibrations in *nc*-rutile TiO_2:Fe films has been studied. The three first-order Raman-active and three infrared-active phonon modes can be observed from the present experimental configuration. It is found that the frequency shifts of the Raman modes are sensitive to the Fe-doping levels and the peak broadening of the infrared-active modes is sensitive to the lattice mismatch and intracrystalline defects, respectively. Moreover, the dielectric functions in the NIR-UV photon energy region have been uniquely extracted by fitting the measured ellipsometric data with a four-phase layered model. The real part of the dielectric functions linearly decreases with increasing Fe composition due to the crystalline structure, the grain size, and the Fe dopants. In the *nc*-TiO_2:Fe films, the Fe introduction is considered to be one of the most important factors to affect the lattice vibration and optical properties such as Raman phonon modes, optical constants, and optical band gap, which linearly decreases from 3.43 to 3.39 eV with the Fe composition. The present results could be crucial for future applications of TiO_2-based optoelectronic and diluted magnetic semiconductor devices.

Acknowledgment. One of the authors (J.Z.Z.) is grateful to Professor Xiaodong Tang, Wenwu Li, Junyu Zhu, Wenlei Yu, and Wenfei Xu for the technical support. This work is financially sponsored in part by Natural Science Foundation of China (Grant No. 60906046), National Basic Research Program of China (Grant Nos. 2007CB924901, 2007CB924902, and 2011CB922202), Program of New Century Excellent Talents, MOE (Grant No. NCET-08-0192), Shanghai Municipal Commission of Science and Technology Project (Grant Nos. 10DJ1400201, 08JC1409000, 08520706100, and 09ZZ42), and the Fundamental Research Funds for the Central Universities.

References and Notes

(1) Mitev, P. D.; Hermansson, K.; Montanari, B.; Refson, K. *Phys. Rev. B* **2010**, *81*, 134303.
(2) Zhou, S.; Čižmár, E.; Potzger, K.; Krause, M.; Talut, G.; Helm, M.; Fassbender, J.; Zvyagin, S. A.; Wosnitza, J.; Schmidt, H. *Phys. Rev. B* **2009**, *79*, 113201.
(3) Hong, N. H.; Sakai, J.; Poirot, N.; Brizé, V. *Phys. Rev. B* **2006**, *73*, 132404.
(4) Lee, C.; Ghosez, P.; Gonze, X. *Phys. Rev. B* **1994**, *50*, 13379.
(5) Fujishima, A.; Honda, K. *Nature* **1972**, *238*, 37.
(6) Pearton, S. J.; Heo, W. H.; Ivill, M.; Norton, D. P.; Steiner, T. *Semicond. Sci. Technol.* **2004**, *19*, R59.
(7) Carbone, R.; Marangi, I.; Zanardi, A.; Giorgetti, L.; Chierici, E.; Berlanda, G.; Podestà, A.; Fiorentini, F.; Bongiorno, G.; Piseri, P.; Pelicci, P. G.; Milani, P. *Biomaterials* **2006**, *27*, 3221.
(8) Tsunekawa, S.; Ishikawa, K.; Li, Z. Q.; Kawazoe, Y.; Kasuya, A. *Phys. Rev. Lett.* **2000**, *85*, 3440.
(9) Yahia, M. B.; Lemoigno, F.; Beuvier, T.; Filhol, J. S.; Richard-Plouet, M.; Brohan, L.; Doublet, M. L. *J. Chem. Phys.* **2009**, *130*, 204501.
(10) Shirley, R.; Kraft, M.; Inderwildi, O. R. *Phys. Rev. B* **2010**, *81*, 075111.
(11) Jellison, J. G. E.; Boatner, L. A.; Budai, J. D.; Jeong, B. S.; Norton, D. P.; Swamy, V. *J. Appl. Phys.* **2003**, *93*, 9537.
(12) Swamy, V.; Muddle, B. C.; Dai, Q. *Appl. Phys. Lett.* **2006**, *89*, 163118.
(13) Swamy, V. *Phys. Rev. B* **2008**, *77*, 195414.
(14) Hu, Z. G.; Li, W. W.; Wu, J. D.; Sun, J.; Shu, Q. W.; Zhong, X. X.; Zhu, Z. Q.; Chu, J. H. *Appl. Phys. Lett.* **2008**, *93*, 181910.
(15) Schilfgaarde, M. V.; Kotani, T.; Faleev, S. *Phys. Rev. Lett.* **2006**, *96*, 226402.
(16) Chiodo, L.; García-Lastra, J. M.; Iacomino, A.; Ossicini, S.; Zhao, J.; Petek, H.; Rubio, A. *Phys. Rev. B* **2010**, *82*, 045207.
(17) Rangan, S.; Katalinic, S.; Thorpe, R.; Bartynski, R. A.; Rochford, J.; Galoppini, E. *J. Phys. Chem. C* **2010**, *114*, 1139.
(18) Mo, S. D.; Ching, W. Y. *Phys. Rev. B* **1995**, *51*, 13023.
(19) Matsumoto, Y.; Murakami, M.; Shono, T.; Hasegawa, T.; Fukumura, T.; Kawasaki, M.; Ahmet, P.; Chikyow, T.; Koshihara, S. y.; Koinuma, H. *Science* **2001**, *291*, 854.
(20) Sangaletti, L.; Mozzati, M. C.; Galinetto, P.; Azzoni, C. B.; Speghini, A.; MBettinelli; Calestani, G. *J. Phys.: Condens. Matter* **2006**, *18*, 7643.
(21) Coey, J. M. D.; Venkatesan, M.; Fitzgerald, C. B. *Nat. Mater.* **2005**, *4*, 173.
(22) Yamaura, K.; Wang, X. H.; Li, J. G.; Ishigaki, T.; Takayama-Muromachi, E. *Mater. Res. Bull.* **2006**, *41*, 2080.
(23) Choi, W.; Termin, A.; Hoffmann, M. R. *J. Phys. Chem.* **1994**, *98*, 13669.
(24) Hu, Z. G.; Li, Y. W.; Zhu, M.; Zhu, Z. Q.; Chu, J. H. *J. Phys. Chem. C* **2008**, *112*, 9737.
(25) Gopalan, R.; Lin, Y. S. *Ind. Eng. Chem. Res.* **1995**, *34*, 1189.
(26) Zhu, J.; Ren, J.; Huo, Y.; Bian, Z.; Li, H. *J. Phys. Chem. C* **2007**, *111*, 18965.
(27) Tompkins, H. G.; Tiwald, T.; Bungay, C.; Hooper, A. E. *J. Phys. Chem. B* **2004**, *108*, 3777.
(28) Azzam, R. M. A.; Bashara, N. M. *Eillipsometry and Polarized light*; North-Holland: Amsterdam, The Netherlands, 1977.
(29) Li, W. W.; Hu, Z. G.; Wu, J. D.; Sun, J.; Zhu, M.; Zhu, Z. Q.; Chu, J. H. *J. Phys. Chem. C* **2009**, *113*, 18347.
(30) Yu, W. L.; Li, W. W.; Wu, J. D.; Sun, J.; Zhu, J. J.; Zhu, M.; Hu, Z. G.; Chu, J. H. *J. Phys. Chem. C* **2010**, *114*, 8593.
(31) Li, W. W.; Hu, Z. G.; Li, Y. W.; Zhu, M.; Zhu, Z. Q.; Chu, J. H. *ACS Appl. Mater. Interfaces* **2010**, *2*, 896.
(32) Patterson, A. L. *Phys. Rev.* **1939**, *56*, 978.
(33) Bai, W.; Meng, X. J.; Lin, T.; Tian, L.; Jing, C. B.; Liu, W. J.; Ma, J. H.; Sun, J. L.; Chu, J. H. *J. Appl. Phys.* **2009**, *106*, 124908.
(34) Chen, Y.; Zhou, X.; Zhao, X.; He, X.; Gu, X. *Mater. Sci. Eng., B* **2008**, *151*, 179.
(35) Bersani, D.; Lottici, P. P.; Ding, X. Z. *Appl. Phys. Lett.* **1998**, *72*, 73.
(36) Zhang, J.; Li, M.; Feng, Z.; Chen, J.; Li, C. *J. Phys. Chem. B* **2006**, *110*, 927.
(37) Hu, Z. G.; Weerasekara, A. B.; Dietz, N.; Perera, A. G. U.; Strassburg, M.; Kane, M. H.; Asghar, A.; Ferguson, I. T. *Phys. Rev. B* **2007**, *75*, 205302.
(38) Nomoto, T.; Sasahara, A.; Onishi, H. *J. Chem. Phys.* **2009**, *131*, 084703.

(39) Parker, J. C.; Siegel, R. W. *Appl. Phys. Lett.* **1990**, *57*, 943.
(40) Mazza, T.; Barborini, E.; Piseri, P.; Milani, P.; Cattaneo, D.; Li Bassi, A.; Bottani, C. E.; Ducati, C. *Phys. Rev. B* **2007**, *75*, 045416.
(41) Balcells, L.; Frontera, C.; Sandiumenge, F.; Roig, A.; Martinez, B.; Kouam, J.; Monty, C. *Appl. Phys. Lett.* **2006**, *89*, 122501.
(42) Gao, Y. Q.; Huang, Z. M.; Hou, Y.; Wu, J.; Ge, Y. J.; Chu, J. H. *Appl. Phys. Lett.* **2009**, *94*, 011106.
(43) Palik, E. D. *Handbook of Optical Constants of Solid*; Academic: New York, 1985.
(44) Adachi, S. *Phys. Rev. B* **1987**, *35*, 7454; **1988**, *38*, 12345.
(45) Bruggeman, D. A. G. *Ann. Phys. (Leipzig)* **1935**, *24*, 636.
(46) Fujiwara, H.; Koh, J.; Rovira, P. I.; Collins, R. W. *Phys. Rev. B* **2000**, *61*, 10832.
(47) Herzinger, C. M.; Johs, B.; McGahan, W. A.; Woollam, J. A.; Paulson, W. *J. Appl. Phys.* **1998**, *83*, 3323.
(48) Press, W. H.; Teukolsky, S. A.; Vetterling, W. T.; Flannery, B. P. *Numerical Recipes in C: The Art of Scientific Computing*; Cambridge University Press: Cambridge, MA, 1992.
(49) Dow, J. D.; Redfield, D. *Phys. Rev. B* **1972**, *5*, 594.
(50) Suzuki, M.; Ohdaira, H.; Matsumi, T.; Kumeda, M.; Shimizu, T. *J. Appl. Phys.* **1977**, *16*, 221.
(51) Nagaveni, K.; Hegde, M. S.; Madras, G. *J. Phys. Chem. B* **2004**, *108*, 20204.
(52) Graetzel, M.; Howe, R. F. *J. Phys. Chem.* **1990**, *94*, 2566.

JP1056286